# Chapter 6
# Empirical Model Calibration

The concept of empirical density model calibration was introduced in Sect. 2.5. This chapter will provide some details on an implementation of this technique, as developed under contract for the European Space Operations Centre [7, 8, 11].

Section 6.1 gives a mathematical description of the approach, introducing two different calibration parameterisation schemes. Implementations of these parameterisations have been tested using density data derived from TLEs and accelerometer data. These tests and their results are discussed in Sects. 6.2 and 6.3, respectively.

## 6.1 Estimation, Model Parameterisation and Data Preparation

The estimation of density calibration parameters is based on least-squares adjustment, using the Levenberg-Marquardt algorithm [1, 18, 20], in order to minimise the difference between observed density values derived from satellite drag and their equivalent values computed using the parameterised model. The Levenberg-Marquardt algorithm interpolates between the method of gradient descent and the inverse-Hessian method. The algorithm therefore requires the parameterised model implementation to return the Jacobian matrix, containing the partial derivatives of the density with respect to the calibration parameters, as well as the density itself.

### *6.1.1 Parameterisation Methods*

The next paragraphs will present the two ways of parameterising the density model that have been implemented and tested.

**Height-Dependent Model Density Scale Factors**

If the unadjusted empirical model density is designated $\rho_m$, then an adjusted model can be calculated by multiplying this value with a scale factor $f$. This scale factor $f$ can be a function in three-dimensional space, expressed in height $h$ above the Earth's

E. Doornbos, *Thermospheric Density and Wind Determination from Satellite Dynamics*, Springer Theses, DOI: 10.1007/978-3-642-25129-0_6,

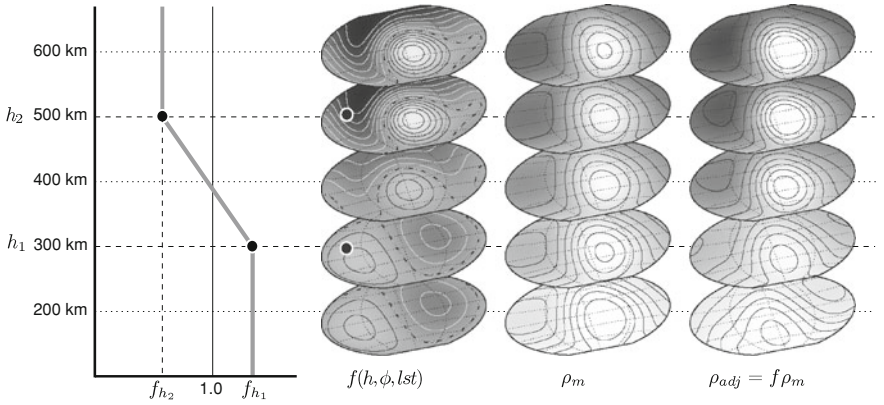


**Fig. 6.1** Illustration of the height-dependent scale factor calibration scheme, using two height levels, at 300 and 500 km, with spherical harmonic expansions up to degree and order 1 and 2, at each height level, respectively

surface, latitude $\phi$ and local solar time $\lambda_\odot$.

$$\rho_{adj} = f(h, \phi, \lambda_\odot) \cdot \rho_m \tag{6.1}$$

The height variation of $f$ is accomplished by a piecewise-linear interpolation between a set of $N_{f_h}$ scale factors $f_{h_i}$ at predefined reference heights $h_i$. Above and below the bottom- and top-most reference height ($h_1$ and $h_N$, respectively), the scale factor is kept constant.

$$f = \begin{cases} f_{h_1} & \text{if } h < h_1 \\ f_{h_i} + \frac{h-h_i}{h_{i+1}-h_i}(f_{h_{i+1}} - f_{h_i}) & \text{if } h_i \le h \le h_{i+1} \text{ for } i = 1, \ldots, N_{f_h} - 1 \\ f_{h_N} & \text{if } h > h_N \end{cases} \tag{6.2}$$

This equation is illustrated on the left-hand side of Fig. 6.1. If $N_{f_h}$ equals one, there is no height-dependence in the correction, and the value of $h_1$ is irrelevant.

This scheme is an enhanced version of the method used by Yurasov et al. [23], in which a two-parameter correction corresponding to a scale factor with a slope in height was estimated. In their method, the density multiplication factor will reach unrealistic values at low and high altitudes. Therefore, such an adjustment could easily result in invalid density values above and below the perigee height range of the calibration data, even though the original unadjusted model could still return reasonable values there. Using Equation (6.2), this behaviour is avoided if the heights $h_i$ are set within the height span of the calibration data.

The height levels offer the possibility of adding spatial resolution of the density correction function in the vertical direction. In order to accommodate spatial variations in the horizontal plane, each height-dependent scale factor $f_{h_i}$ can be expanded in a set of spherical harmonics in latitude $\phi$ and local solar time $\lambda_\odot$. This allows

**Table 6.1** Sets of spherical harmonic parameters used in the calibration tests, with their number of parameters $N$ and names used in the discussion of these tests

| Name | N | Spherical harmonic coefficients |
|---|---|---|
| Global | 1 | $C_{00}$ |
| Offset | 4 | $C_{00}$, $C_{10}$, $C_{11}$, $S_{11}$ |
| Zonal | 4 | $C_{00}$, $C_{10}$, $C_{20}$, $C_{30}$ |
| Bulge | 9 | $C_{00}$, $C_{10}$, $C_{11}$, $S_{11}$, $C_{20}$, $C_{21}$, $S_{21}$, $C_{22}$, $S_{22}$ |

spatial features in horizontal planes around the Earth to be represented using the equation:

$$f_{h_i} = C_{00}^{h_i} + \sum_{n=1}^{N_{h_i}} \left[ \sum_{m=0}^{n} C_{nm}^{h_i} P_{nm}(\sin\phi)\cos(m\lambda_{\odot}) + \sum_{m=1}^{n} S_{nm}^{h_i} P_{nm}(\sin\phi)\sin(m\lambda_{\odot}) \right] \tag{6.3}$$

The spherical harmonic coefficients $C_{nm}^{h_i}$ and $S_{nm}^{h_i}$ are the model parameters that are to be estimated. $P_{nm}$ are the unnormalised associated Legendre functions of degree $n$ and order $m$ (e.g., [19]).

The low degree and order spherical harmonic coefficients have a clear physical meaning: $C_{00}$ is a global scale factor. Its default value, for an unadjusted model, should be set to one. The higher degree and order coefficients are the ones that allow for variation around this mean in the horizontal plane, and their default value in an unadjusted model is zero. The three components of degree and order 1 allow for an offset with respect to the geocenter: $C_{11}$ for the X-direction, $S_{11}$ for Y and $C_{10}$ for Z. Zonal coefficients, for which $m = 0$, can represent variations in latitude only: $C_{20}$ introduces a flattening (ellipsoidal instead of spherical shape) and $C_{30}$ a hemispherical asymmetry with respect to the equator (pear-shape).

Figure 6.1 illustrates the calibration scheme. In this specific example, a linear interpolation is used between two height levels, at 300 and 500 km altitude. At the lower level, a spherical harmonic expansion up to degree and order 1 is used, while at the higher level, where observation data is usually more abundant, the expansion is to degree and order 2. Using such low order spherical harmonics, the shape, position and amplitude of the diurnal density bulge can be easily modified. If data of sufficient coverage and accuracy are available, higher order spherical harmonics can be used to represent shorter wavelength density fluctuations.

A number of named sets of spherical harmonic parameters are listed in Table 6.1. These will be referred to later on in the chapter, when the effectiveness of the various sets of parameters is evaluated.

### CIRA-72 temperature corrections

A second parameterisation method that was implemented involves the use of CIRA-72 temperature corrections. The scheme is based on the Dynamic Calibration Atmosphere (DCA) used in the HASDM project [3, 5].

Since the scheme requires a modification of the internals of the Jacchia model, we will refer to Sect. 2.4.1, which introduced the relation between several temperature parameters and the density output. As explained there, vertical density profiles at a given location are computed by integrating the hydrostatic and diffusion equations from the lower boundary conditions, based on a temperature profile with altitude that is a function of two pre-computed temperatures: $T_x$ at 125 km, which is the temperature inflection point in the uncalibrated model, and $T_\infty$ as the asymptotic maximum temperature at the top of the atmosphere.

In order to calibrate the model, corrections to these temperatures, $\Delta T_x$ and $\Delta T_\infty$, are both expanded in spherical harmonics, in a similar manner as the height-dependent scale factors of Equation (6.3). The set of spherical harmonic coefficients of these temperature corrections, $C_{nm}^{T_x}$, $S_{nm}^{T_x}$, $C_{nm}^{T_\infty}$ and $S_{nm}^{T_\infty}$, can then be estimated during the calibration procedure.

The resulting corrections $\Delta T_\infty$ and $\Delta T_x$ are added to the Equations (2.8) and (2.9), as follows:

$$T_\infty = T_c D + \Delta T_G + \Delta T_\infty \tag{6.4}$$

$$T_x = a + bT_\infty + c\exp(kT_\infty) + \Delta T_x \tag{6.5}$$

The complete temperature profile and local densities are then computed using the standard model formulations, as explained in Sect. 2.4.1. Figure 6.2 illustrates the influence of the calibration parameters on the temperature and density profiles of the CIRA-72 model. Note that the inflection point of the temperature profile moves to a lower altitude than 125 km, if the temperature $T_x$ at that altitude is adjusted to a higher value, and vice versa, so that while we will keep the notation, technically the adjusted $T_x = T_{125\,\mathrm{km}}$ is no longer the inflection point temperature.

**Advantages and Disadvantages of the Two Calibration Methods**

A theoretical disadvantage of the temperature correction method is that adjustments can only be made with two degrees of freedom in the vertical. In reality, due to sparseness of data, it has not been possible to test adjustments at more than two height levels in any case. A benefit of the temperature calibration scheme over the scale factor scheme is that the estimated parameters have a physical meaning in the model. The scale factors apply only to the total neutral density. Therefore, the temperature and composition results of the original model remain unaffected by the scale factors, and are no longer physically coherent with the scaled total density. In contrast, the corrected temperatures are at the basis of the CIRA-72 model, in which density and composition are computed based on physical principles from these temperatures.

Note however that the value of the corrected temperature $T_x$ at 125 km should not be interpreted as representing the true temperature at this altitude. The uncorrected temperature parameter is closely tied to the lower boundary conditions of the CIRA-72 model, and its correction will be extrapolated from drag data above 200 km

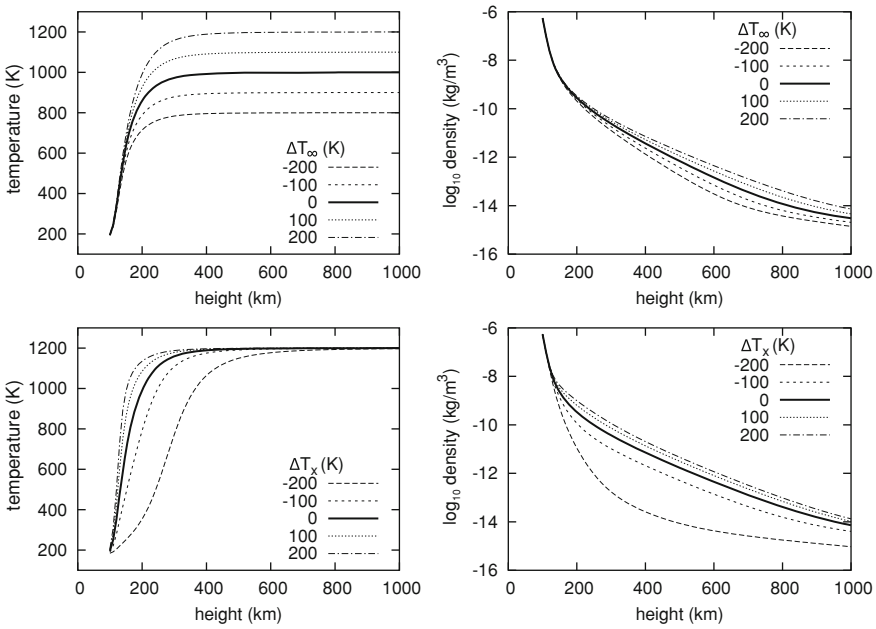


**Fig. 6.2** Vertical profiles of density and temperature for various values of the calibration corrections for the inflection point and exospheric temperatures

through the temperature-density relations of the model, both of which will introduce considerable uncertainties.

## *6.1.2 Selection and Preparation of Density Data*

The Levenberg-Marquardt algorithm is applied to minimise the difference between observed and equivalent model densities, divided by a weighting factor. The following sections will show how to arrive at these values, covering aspects of data selection, weighting and optimisation of computation time.

### TLE-Derived Densities

The TLE-derived observed density data for calibration are obtained by evaluating Equation (4.6). Equation (4.7) can then be used to arrive at equivalent model values. Unfortunately, Equation (4.7) requires many calls to the density model per data point, because of the need to integrate the density over the satellite trajectory. In addition, the partial derivatives of the density with respect to the calibration parameters need to be integrated in a similar manner. This can be time consuming. Fortunately, the computations can be significantly speeded up by storing the intermediate calculation

**Table 6.2** Characteristics of the selected validation objects, from left to right: NORAD identifier, SATCAT name, launch date, decay date, inclination, perigee and apogee height ranges (km) for the year 2000, and ballistic coefficient (kg/m$^2$)

| ID | Name | Launch | Decay | $i$ | $h_p$ | $h_a$ | B |
|---|---|---|---|---|---|---|---|
| 22875 | COSMOS 2265 | 1993/10/26 | 2003/08/11 | 82.9° | 287–279 | 1239–1084 | 123.45 |
| 2389 | OV3-3 | 1966/08/04 | – | 81.4° | 350–347 | 2977–2899 | 57.14 |
| 4382 | DFH-1 | 1970/04/24 | – | 68.4° | 431–431 | 2143–2124 | 93.46 |
| 2611 | OV1-10 | 1966/12/11 | 2002/11/30 | 93.4° | 516–495 | 583–545 | 43.10 |
| 63 | TIROS 2 | 1960/11/23 | – | 48.5° | 535–523 | 592–574 | 69.93 |

results that are independent of the values of the calibration parameters, in computer memory or on disk.

Several aspects of the TLE data editing and selection process were already presented in Sect. 4.1.4. The next paragraph provides some further details on these aspects pertaining to the density model calibration tests.

An initial list of suitable calibration objects, used in the HASDM project, was kindly provided by Bruce Bowman (2005, personal communication). The densities were at first computed over the irregular integration time spans between pairs of TLE data. A minimum integration time span of half a day and a maximum of five days were used. Daily values for use in the daily density adjustment were calculated as an average of the collection of values valid for overlapping time spans. This introduces some smoothing in the process. Objects and time periods for which the effects of solar radiation pressure on the orbit are not negligible compared to drag, or where orbit differences between adjacent TLEs are excessively large, have been eliminated from further data processing. Ballistic coefficients were calculated under the assumption that the long-term average of the ratio of observed to modeled density ratios should equal one. The resulting ballistic coefficient values were generally found to be within 5% of values found in other research [2, 13, 17].

Depending on TLE data availability, either 48 or 49 objects, with a perigee range of approximately 180–550 km, were used to provide density estimates for each of the 366 days in 2000. These data were used as input to the 366 daily estimations of model parameters. The TLE-derived density data of five additional objects at different perigee altitudes were deliberately not used in the density calibration. Their data are used to independently assess the performance of the models. The validation satellites are listed in Table 6.2. In the presentation of results, they will be referred to by their name and approximate perigee height.

### Accelerometer-Derived Densities

Accelerometer-derived densities as inputs to the calibration have been derived using Equation (4.12) for GRACE and Equation (4.28) for CHAMP. The accelerometer-derived data can be considered to consist of instantaneous measurements of the density, so they can simply be compared to the output of the parameterised density model evaluated at the same time and location.

Accelerometer data from CHAMP and GRACE are available at least every 10 s. In order to speed up the computation process when using accelerometer-derived data, it is beneficial to reduce the data amount, at the cost of some temporal and spatial resolution. This data reduction, either by averaging data into normal points, or by simply skipping data, can be tuned to match the temporal and spatial resolution that can be resolved by the chosen model parameterisation.

**Data Weighting**

Each data point derived from TLE s has been given a weight, which is inversely proportional to a fixed fraction (e.g. 10%) of the observed density. This ensures that high altitude and nighttime data gets sufficient relative weight in the adjustment. For these circumstances, the absolute density, and therefore also the density residual, is already small compared to data obtained at lower altitudes and during the daytime.

The data weighting for accelerometer data is based on an error analysis, similar to the one presented in Sect. 4.2.4. Details are available in Doornbos et al. [12]. Such more sophisticated data weighting schemes, based on an assessment of the relative accuracy of data obtained from different sources or conditions, is likely to be of benefit for the accuracy of the model calibrated using TLE data as well. This is foreseen to be part of future activities.

The combined adjustment of calibration parameters using both TLE- and accelerometer-derived data would also be of great interest, since the temporal and spatial resolutions of both methods could complement each other. This would, however, present an additional challenge regarding optimal relative data weighting and is left as a topic for future research.

## 6.2 Calibration Tests Using TLE Data

The evaluation of the density calibration procedure using TLE data consists of three parts. In the first part, we will look at time series of temperature adjustments. In the second part, the implementation of the estimation of spherical harmonic coefficients is checked, using maps of modeled density at 500 km altitude. In the third and final part, we will directly compare the performance of the different calibration schemes and number of spherical harmonic coefficients, using all five validation objects. In addition, the adjusted models are evaluated in the precise orbit determination of the ERS-2 satellite.

**Time Series of Calibration Parameters and Density Ratios**

A time series of estimated CIRA-72 temperature corrections is shown in Fig. 6.3, panel (b). Only the $C_{00}$, or global terms (see Table 6.1), of these corrections have been estimated. The variations can be compared with variations in $F_{10.7}$ and $a_p$ in panel (a), which are the parameters used to determine the uncorrected temperatures in the CIRA-72 model. Large jumps in $\Delta T_\infty$, especially in July and August, coincide with

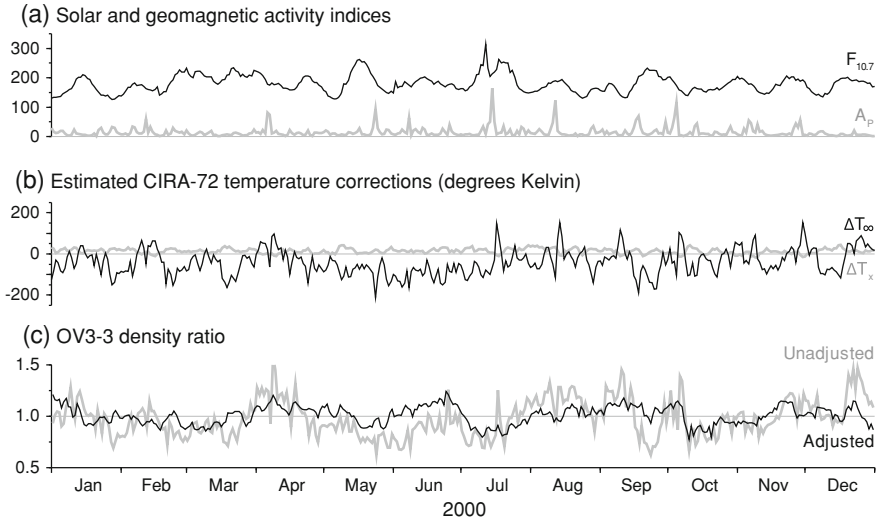


**Fig. 6.3** Time-series of **a** $F_{10.7}$ solar flux and the $A_p$ daily planetary geomagnetic index; **b** Estimated global CIRA-72 temperature corrections $\Delta T_x$ and $\Delta T_\infty$ in degrees Kelvin; and **c** Ratio of modeled over observed densities encountered by the OV3-3 satellite, for both the unadjusted CIRA-72 model, and the CIRA-72 model with the two global temperature corrections of panel (**b**) applied

large geomagnetic storms. Variations with a periodicity of approximately 27-days, similar to that in $F_{10.7}$ are also present. The temperature corrections therefore show variations that can be related to deficiencies in the representation of both geomagnetic and solar activity variations. Over the entire year, corrections to $T_\infty$ are predominantly negative, while corrections to $T_x$ are positive and much lower in amplitude. The two parameters often show an anti-correlated behaviour. The bottom panel of Fig. 6.3 makes a comparison of observed over modeled density ratios for the OV3-3 satellite, which is one of the validation objects listed in Table 6.2. The time series for the adjusted model clearly stays closer to the ideal ratio of 1 and shows less variability than for the unadjusted model. Indeed, the RMS relative density error was reduced from 19.8 to 9.2%. This indicates that the calibration was successful in lowering the model error.

### Density Maps

Figure 6.4 shows the effect of adding higher degree and order spherical harmonic coefficients to the density calibration parameter estimation. The figure compares maps of modeled density at 500 km altitude for unadjusted and adjusted versions of CIRA-72 and MSIS. The spherical harmonic expansion in the adjusted model was up to degree and order 2 for $T_\infty$ and $f_{500}$, respectively (corresponding to the keyword "bulge" in Table 6.1). Only a degree and order 0 (global) term was used for the low altitude parameters $T_x$ and $f_{300}$. However, these parameters do not or hardly affect the density output at 500 km and above.

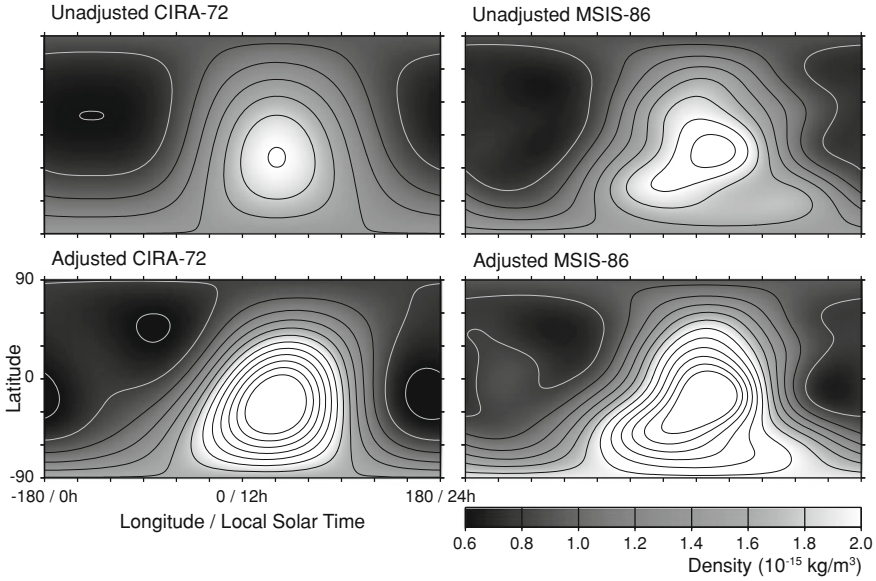


**Fig. 6.4** Maps of modeled density at 500 km altitude at 12:00:00 UTC on January 16, 2000. The *top row* shows the output of traditional empirical models: CIRA-72 and MSIS-86. The *bottom row* shows the output of these models, calibrated using degree and order 2 spherical harmonics

A comparison of the top two frames of the figure shows that the MSIS-86 model shows a more detailed and asymmetrical picture of the diurnal bulge. This asymmetry had not yet been resolved from the rather sparse observation data at the time CIRA-72 was created. After adjustment however, both models show a much more similar picture. It appears that the asymmetrical shape of the diurnal bulge, which was already present in the MSIS model is indeed correct in this situation. It is also clear that both adjusted models show a much higher amplitude of the maximum day-time density than their unadjusted counterparts, even though the minimum density remains about the same for this epoch and altitude.

### Comparison of Parameterisation Schemes

Table 6.3 contains a comparison of the performance of various density calibration schemes, in terms of the RMS of the relative density error (see Sect. 2.6.2), with respect to data from five validation satellites. The data from the validation satellites were not used in the adjustments of the models. The table contains three sections: several combinations of spherical harmonic expansions of scale factors have been applied to both the NRLMSIS-00 model and to CIRA-72, while the latter model has been tested with temperature corrections as well. The top row of each section contains the statistics of the unadjusted model.

Figure 6.5 contains a bar chart representation of the top and bottom rows of each section from this table. These relative RMS differences between TLE-derived and

**Table 6.3** Comparison of adjusted empirical density models. N is the total number of estimated parameters (see Table 6.1). The other numbers show the RMS of the relative density errors, for the selected validation satellites over the year 2000. Lower values indicate better performance

| | | | COSMOS 2265 280 km | OV3-3 350 km | DFH-1 430 km | OV1-10 500 km | TIROS 2 530 km |
|---|---|---|---|---|---|---|---|
| $f_{300}$ | $f_{500}$ | N | *NRLMSISE-00* adjusting scale factors $f_{300}$ and $f_{500}$ | | | | |
| – | – | 0 | 10.4 | 16.3 | 27.8 | 27.9 | 24.9 |
| Global | – | 1 | 9.4 | 8.3 | 16.3 | 11.3 | 11.3 |
| Global | Global | 2 | 5.4 | 8.1 | 14.9 | 7.9 | 9.1 |
| Global | Zonal | 5 | 5.4 | 7.8 | 14.2 | 9.6 | 9.2 |
| Zonal | Zonal | 8 | 11.6 | 8.4 | 13.8 | 10.0 | 9.3 |
| Global | Bulge | 10 | 5.3 | 7.3 | 9.9 | 11.0 | 9.1 |
| $f_{300}$ | $f_{500}$ | N | *CIRA*-72 adjusting scale factors $f_{300}$ and $f_{500}$ | | | | |
| – | – | 0 | 12.7 | 19.8 | 33.1 | 34.5 | 28.3 |
| Global | – | 1 | 11.5 | 9.6 | 18.7 | 12.9 | 11.1 |
| Global | Global | 2 | 7.7 | 9.8 | 17.1 | 7.6 | 11.5 |
| Global | Zonal | 5 | 7.5 | 9.4 | 16.1 | 7.7 | 10.8 |
| Zonal | Zonal | 8 | 16.0 | 9.7 | 15.7 | 8.4 | 10.7 |
| Global | Bulge | 10 | 7.4 | 8.3 | 10.3 | 8.9 | 9.8 |
| $\Delta T_x$ | $\Delta T_\infty$ | N | *CIRA*-72 adjusting temperatures $T_x$ and $T_\infty$ | | | | |
| – | – | 0 | 12.7 | 19.8 | 33.1 | 34.5 | 28.3 |
| – | Global | 1 | 9.0 | 9.5 | 16.7 | 8.9 | 9.3 |
| Global | Global | 2 | 8.1 | 9.2 | 15.6 | 7.9 | 11.5 |
| Global | Zonal | 5 | 7.1 | 8.7 | 14.3 | 7.7 | 10.7 |
| Zonal | Zonal | 8 | 9.3 | 8.9 | 13.9 | 8.6 | 10.4 |
| Global | Bulge | 10 | 6.9 | 8.7 | 11.5 | 8.0 | 9.5 |

modeled density values contain the contributions of the errors in the density model we are interested in, but they also contain any errors in the TLE to density processing. Based on analysis of our ballistic coefficient estimates and density adjustment results, these density observation errors are expected to be at a level of around 5% RMS at low altitude and high solar activity. At lower solar activity or higher altitudes, this error quickly increases (see Fig. 5.9). The limited temporal resolution of the TLE-derived data, as discussed in Sect. 4.1, should also be kept in mind when interpreting these numbers.

The RMS differences for the unadjusted models in Table 6.3 and Fig. 6.5 are between 10–13% at 280 km and 25–35% above 430 km, well above the estimate of the error in the validation observations. These numbers are therefore mainly an indication of the level of error in the unadjusted models. The more recent NRLMSIS-00 model performs better than CIRA-72 when both models are uncalibrated. The estimation of a single global calibration parameter per day, however, already improves the accuracy of both models by a great deal, to around 9–19% RMS. Adding the second global parameter, or increasing the number of spherical harmonic coefficients, brings the RMS error further down by more modest amounts. The global–bulge combination

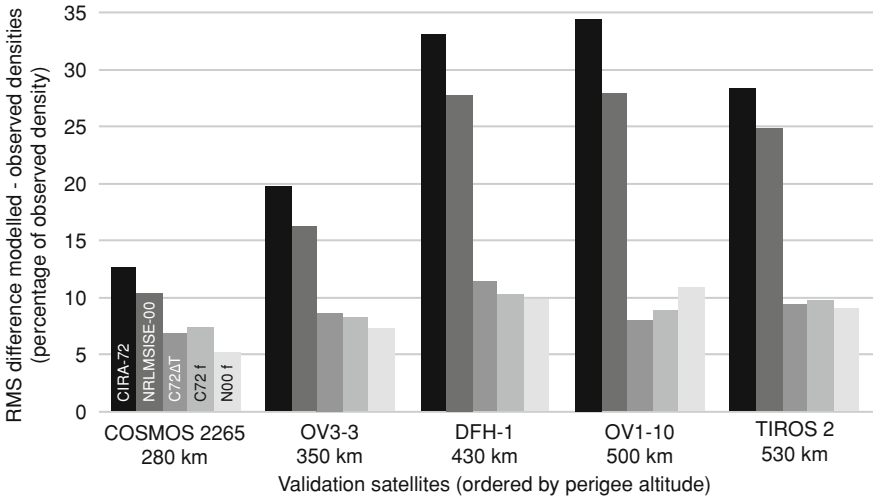


**Fig. 6.5** *Bar graph* showing the increase in accuracy due to model calibration, using the data from Table 6.3. The calibrated models were adjusted using the global–bulge spherical harmonic combination of ten parameters representing temperature adjustments ($\Delta T$) or scale factors ($f$)

is the most effective, bringing the RMS error down to 5–11% RMS, close to the estimated error level of the validation observations.

The zonal–zonal results, based on eight parameters, are generally worse than the global-zonal and global-bulge results, based on five and ten parameters respectively, This indicates that the introduction of additional spherical harmonics at the high altitude level ($f_{500}$ or $T_\infty$) is apparently more effective than at the lower level ($f_{300}$ or $T_x$).

Since the two models are calibrated using the same data, it could be expected that the differences in remaining error between the calibrated models disappears as more parameters are estimated. This is not completely the case, indicating that the calibration parameters and data are not able to capture all density variations. The NRLMSIS-00 model still outperforms CIRA-72, even when ten parameters are adjusted for both models. It should be noted that the MSIS series of models contain much more detail and accuracy at a temporal and spatial resolution beyond that of the calibration data, compared to CIRA-72. This was already evident in Fig. 6.4.

The temperature correction method of CIRA-72, however, delivers slightly better results compared to the scale factor adjustment of the same model, at least when only a few coefficients are estimated. The addition of more spherical harmonic parameters reduces this difference.

Our results over the year 2000 can be compared to those presented for the HASDM test period during the first half of 2001 [4]. The HASDM results are based on 75–80 calibration objects for which Space Surveillance Network tracking data were processed. This has enabled a higher temporal resolution of corrections in HASDM than is available to us through the use of publicly available TLEs, which can be

**Table 6.4** Comparison of gravity field models (top section) and density models (bottom), and their effect on the density error RMS for the year 2003, as well as the ERS-2 orbit error in the crossover RMS for cycle 81. The baseline models are indicated with asterisks (*)

| Gravity model | | Crossover RMS (cm) |
|---|---|---|
| JGM-3 | | 9.04 |
| DGM-E04 | | 6.93 |
| EIGEN-GRACE01S | | 6.59 |
| EIGEN-CG03C* | | 6.47 |
| EIGEN-GL04C | | 6.45 |
| Density model | Relative density error RMS (%) | Crossover RMS (cm) |
| CIRA-72 | 30.8 | 7.03 |
| DTM | 21.8 | 6.73 |
| MSIS | 23.0 | 6.49 |
| DTM-94 | 27.8 | 6.94 |
| JB2006 | 23.3 | 7.06 |
| NRLMSIS-00* | 23.5 | 6.47 |
| Calibrated NRLMSIS-00 | 17.1 | 6.37 |

considered a derived product of this tracking data with accuracy and temporal resolution limitations. The HASDM results presented by Bowman and Storz [4] show density errors at the 6–8% level across all heights from 200 to 800 km, which might be considered to be the best obtainable result using Space Surveillance data with this number of calibration objects.

### Evaluation Using ERS-2 Precise Orbit Determination

An evaluation of the model calibration using the ERS-2 satellite, orbiting at about 800 km, was presented by Doornbos et al. [10]. A brief summary of the results will be given below. The evaluation was performed by implementing several empirical density models, including the "global/bulge" calibrated NRLMSIS model, in the ERS-2 orbit determination software. The orbit determination included the estimation of aerodynamic scale factors from the SLR tracking data, as explained in Sect. 4.3.

The evaluation of density error was made using SLR data from the year 2003, by estimating 6-hourly density scale factors, as explained in Sect. 4.3. Orbit determination arcs containing manoeuvres were eliminated. An evaluation of orbit error using radar altimeter crossover statistics was included as well, using only data from repeat cycle number 81, covering 35 days during January and February of 2003.

Table 6.4 shows that the calibrated NRLMSIS-00 model results in a lower RMS density error: 17.1% compared to 23.5% for the uncalibrated model, even when extrapolating to 800 km altitude. This improvement is considerable, since the TLE data used for calibration were observed over an altitude range of approximately 200–550 km. The temporal resolution of the STR-derived density scale factors, of about 6 h, is also higher than that of the TLE-derived data, which is another factor in explaining the somewhat higher residual RMS relative density error.

The 6-hourly scale factors are effective in removing the effects of long-term errors in the density models during the orbit determination process. It is likely that remaining orbit errors due to density error therefore represent mainly shorter-period errors, such as changes caused by variation in geomagnetic activity, as well as due to sampling of the diurnal density bulge over each orbit.

In order to study the effect of the choice of density model on the orbit quality of ERS-2, the radar altimeter data of this satellite were used as well. The altimeter instrument is intended to measure variations in sea and ice level. However, since the sea level usually does not change by more than several centimetres during periods of just a few days, this measurement can also be used as an independent form of tracking data, to evaluate the orbit error. Altimeter crossover differences are formed by differencing the two altimetric sea level measurements from ascending and descending passes which cross at the same location. Only crossovers over open ocean, with a maximum time difference of 5 days were used. The statistics are derived from 8531 crossover locations. These values contain the sum of the natural sea surface variability and a number of errors in the altimetric processing, of which the orbit accuracy is just one. These numbers can therefore be interpreted to evaluate the relative accuracy of different models used in orbit determination, if this is the only variable that is changed. Lower crossover RMS numbers indicate more accurate orbits. However, the crossover statistics do not give any absolute information on orbit accuracy, since the magnitudes of other contributions are not accurately known.

To provide context, the upper part of Table 6.4 shows a comparison between different gravity models, which have traditionally been the main driver for orbit accuracy improvement of altimeter satellites. The JGM-3 [22] and DGM-E04 [21] models were the state-of-the-art gravity models during the late 1990s, optimised for the TOPEX-Poseidon and ERS-1 missions, respectively. The three generations of EIGEN models are all based on GRACE gravity data. The EIGEN-CG03C model [16] was used in the density analysis. Subsequent generations of GRACEA-based gravity models only provide a modest improvement in ERS-2 orbit accuracy, which indicates that gravity model accuracy for this purpose is converging.

The differences in the altimeter crossover statistics for different density models, on the other hand, do not show such a clear development. The magnitude of the differences between the models indicate that in the GRACEA-era, improvements in density modelling have become more important than improvements in gravity modelling for altimetry satellites at this altitude. For the period under investigation, the calibrated NRLMSIS model shows slightly lower orbit errors in the crossovers than the uncalibrated model, which should result in improved sea and ice level data.

**Conclusions of the Calibration Tests Using TLE Data**

Calibration parameters that are estimated from TLE-derived density data can, to a large extent, compensate for the imperfections in traditional empirical density models at high solar activity.

An analysis of estimated temperature correction time series over the year 2000 shows that the exospheric temperature used in the CIRA-72 model is generally

too high and the temperature at 125 km too low over this period. Variations in the exospheric temperature correction reach amplitudes of several hundreds of degrees Kelvin, while the temperature at 125 km is adjusted by several tens of degrees Kelvin. A spherical harmonic expansion of the calibration parameters in local solar time and latitude can be used to improve the modelling of variations in the horizontal plane, such as the shape of the diurnal bulge.

Using only a single calibration factor per day already improves the RMS of daily integrated densities along the orbit of a validation object from a level of around 30% to below 16%. Further improvements, down to 5–10%, can be obtained by estimating more parameters at an additional height level and in a spherical harmonic expansion of latitude and local solar time.

The estimation of temperature corrections to the CIRA-72 model is preferred when temperature and constituent concentrations, consistent with total neutral density are required from the adjusted model. However, an alternative adjustment using scale factors applied to a more accurate base model, such as NRLMSISE-00, delivers slightly more accurate total densities.

The tests applied to the orbit determination of the ERS-2 satellite leads to the conclusion that the density model calibration using data from much lower altitudes (200–550 km) can still lead to significant density modelling improvements and modest orbit determination improvements at 800 km. This improved orbit determination accuracy has a direct positive effect on the accuracy of altimetric measurements of sea and ice level by European Earth observation satellites such as ERS-2, Envisat and CryoSat.

## 6.3 Calibration Tests Using Accelerometer Data

As mentioned in Sect. 2.5, the density calibration software was adapted to accept density data derived from accelerometer data, as part of an ESA-funded study [12]. CHAMP and GRACE data were used to test the software. The test results will be summarised in three parts. First, the time series of model calibration parameters will be analysed. Afterwards, the calibrated models are evaluated along the CHAMP satellite tracks during a short period surrounding the October 2003 geomagnetic storms. The last section presents calibration statistics for both the CHAMP and GRACE tracks, with both satellites used as either a calibration or validation satellite.

### Time Series of Calibration Parameters

The simplest calibration is the application of a single density scale factor. This scale factor, estimated from the accelerometer data, is then applied to all the density model output. Such a calibration has been performed twice, one time using data from only the CHAMP satellite and one time using only the GRACE satellite data.

The resulting time series are visible in Fig. 6.6a. It is clear that the scale factor time series for both satellites are very similar, even though the satellites are at different

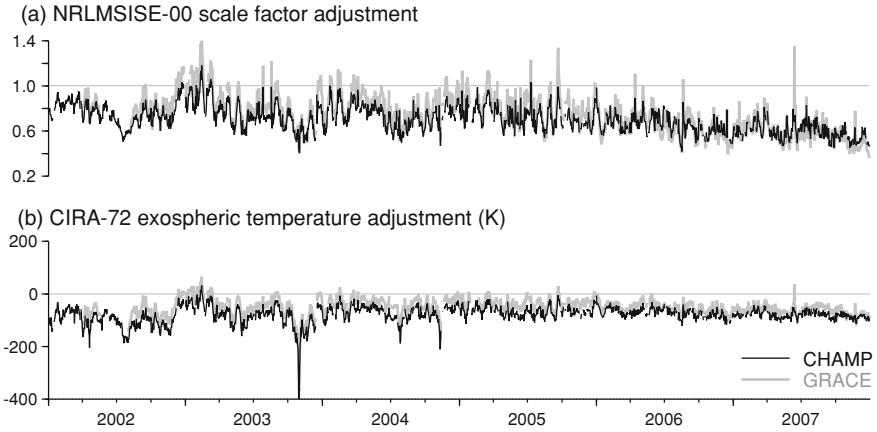


**Fig. 6.6** Estimated density model scale factors ($C_{00}$) for the NRLMSIS-00 model (**a**) and CIRA-72 exospheric temperature adjustments (**b**), comparing values derived solely from CHAMP data (*black line*) and GRACE data (*gray line*)

altitudes, and their local solar time coverage changes continually. This result is in line with the findings from the TLE-derived densities in the previous section. It indicates that there is a large global, time-varying error, which is largely due to the incorrect representation of solar EUV heating (through the $F_{10.7}$ proxy) in the empirical models.

The GRACEA-derived scale factors are a little higher than those from CHAMP, in the earlier years. However, for both satellites, the scale factors are generally below one, indicating that the NRLMSIS-00 model is scaled down, and was originally predicting densities that were too high. At high solar activity, there are large variations at approximately the solar rotation rate, also indicating that the model calibration compensates for inaccurate representation of the solar EUVradiation energy input in the thermosphere. At low solar activity, the scale factor becomes lower and lower. This might be related to the long-term thermospheric cooling trend, which in other analyses was shown to be strongest at solar minimum [14]. This unusual trend during the latest solar minimum was recently investigated in more detail by Emmert et al. [15].

A similar analysis can be made using the CIRA-72 temperature adjustments. Those results are visible in Fig. 6.6b. The discrepancy between the modelled and observed densities translate into an exospheric temperature that is about 100 K lower, than predicted by Jacchia's temperature Equations (2.7) and (2.8), based on $F_{10.7}$ and $a_P$. Note that this mean offset could be attributed to errors in the accelerometer processing, such as the satellite geometry model panel areas, energy accommodation coefficient, etc., as well as to errors in the density model. Note that an offset of the same magnitude is visible both at high solar activity (2002) and at low solar activity (2007). This is in contradiction to Emmert et al. [14, 15], who concluded that a larger temperature difference between data and models exists at solar minimum than

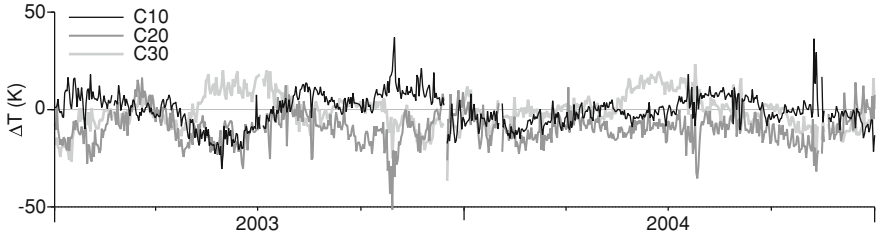


**Fig. 6.7** Estimated zonal components, up to degree 3, of the CIRA-72 exospheric temperature adjustment, using the CHAMP and GRACE data combined

at solar maximum. However, their analysis was based on the NRLMSIS-00 model, not the CIRA-72 model, and they used TLE-derived drag data over a much longer time span, spanning multiple solar cycles. This difference between the two calibration results deserves further investigation.

A large variation of the temperature about this long-term mean can be observed. Its magnitude is about 50–100 K at high solar activity. This variability decreases at low solar activity. A very significant peak of up to −400 K is visible around the time of the October 2003 geomagnetic storms, suggesting that the CIRA-72 model was overestimating the temperature change due to the sudden large additional energy input at that time.

Figure 6.7 shows the exospheric temperature change time series for the CIRA-72 adjustment at the first, second and third order zonal components. Contrary to the previous plots, these values were estimated from the combined processing of CHAMP and GRACE data. The $C_{10}$ and $C_{30}$ components represent a North–South shift, the $C_{20}$ component a shift from the poles to the equator or vice versa. The temperature corrections have an amplitude of about 20–30 K. Large peaks are visible around the October 2003 storm and other solar and geomagnetic activity related events. A larger part of the variation in these time series seems to be at longer wavelengths, such as at the annual and semi-annual periods. This indicates that the calibration adjusts for the inadequate (or non-existing) representation of the coupling between seasonal, local solar time and EUV radiation variation with the diurnal variation in the original CIRA-72 model.

### Calibration Along CHAMP Tracks During the October 2003 Geomagnetic Storm

Figure 6.8 uses the geomagnetic storms at the end of October 2003 as an example to illustrate the model calibration. The top row of the figure shows the observed and uncalibrated model output, sampled along the CHAMP tracks, respectively. The bottom two rows show the output of several calibrated models. The titles for these panels list the base model used for calibration (NRLMSISE-00), the estimation interval (3 h), the spherical harmonic coefficients used as adjustment parameters (either a single scale factor, or an expansion in zonal harmonics up to degree 3),

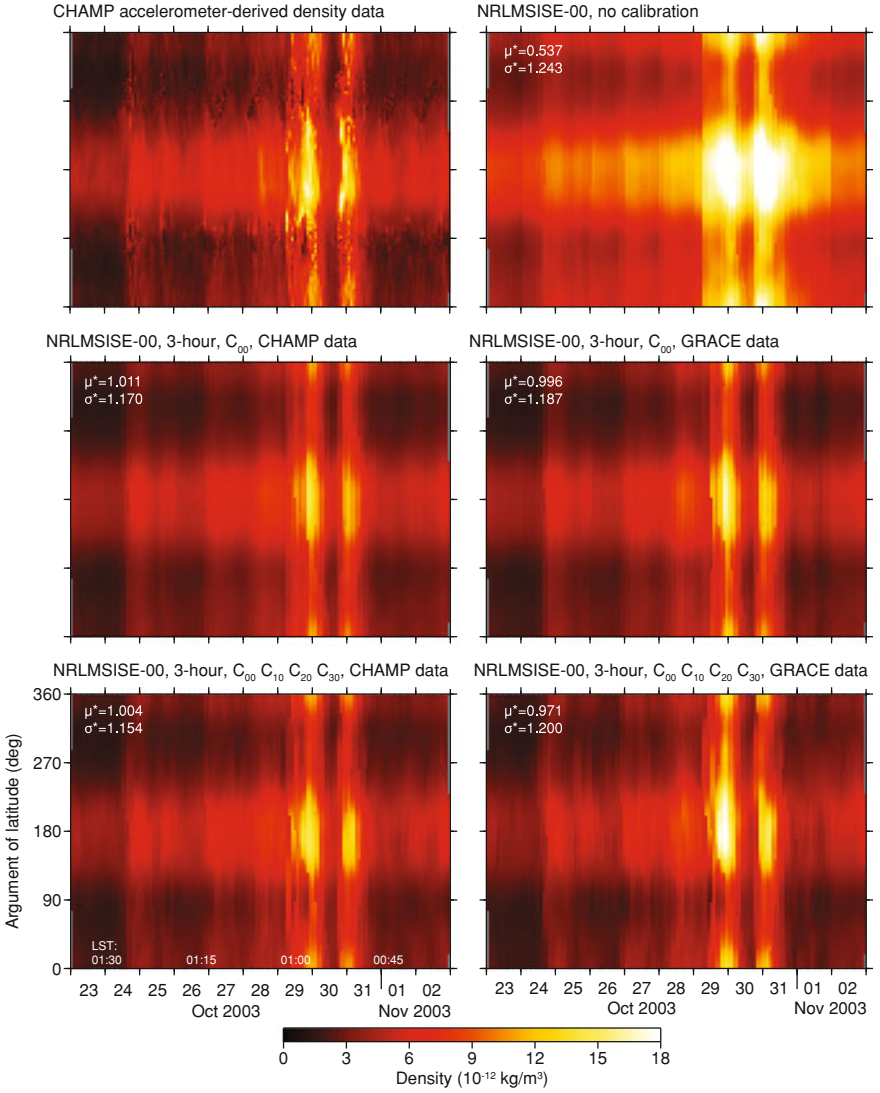


**Fig. 6.8** Comparison of calibrated densities along CHAMP tracks, for the period around the October 2003 geomagnetic storms

and finally the source of density data used in the calibration (either CHAMP or GRACEA). The log-normal mean $\mu^*$ and standard deviation $\sigma^*$, included in each of the plots, are the statistics of the density ratios of the data (top-left) over each of the model values.

The figure shows that in general, as more calibration parameters are added, the model output more closely resembles the CHAMP observation data. While the origi-

**Table 6.5** Statistics of calibrated density model output, evaluated along the CHAMP orbit, over the year 2003. N is the number of measurements used in computing the statistics. $E$ is the RMS of the relative density errors (see Equation (2.15)), and $\mu^*$ and $\sigma^*$ are the log-normal mean and standard deviations of the data/model density ratios

| Base model | Parameters | Interval | N | $E$ (%) | $\mu^*$ | $\sigma^*$ |
|---|---|---|---|---|---|---|
| *Uncalibrated* | | | | | | |
| NRLMSISE-00 | – | – | 3082486 | 47.4 | 0.759 | 1.251 |
| JB-2008 | – | – | 3082486 | 35.0 | 0.803 | 1.193 |
| *HASDM calibrated model using SSN data* | | | | | | |
| HASDM | Custom | 3-hourly | 3082486 | 33.4 | 0.787 | 1.144 |
| *CHAMP data used for calibration* | | | | | | |
| NRLMSISE-00 | $C_{00}$ | Daily | 3082474 | 14.1 | 1.029 | 1.152 |
| NRLMSISE-00 | $C_{00}$ | 3-hourly | 3082472 | 13.0 | 1.024 | 1.138 |
| NRLMSISE-00 | $C_{00}$, $C_{10}$, $C_{20}$, $C_{30}$ | Daily | 3082478 | 13.4 | 1.026 | 1.145 |
| NRLMSISE-00 | $C_{00}$, $C_{10}$, $C_{20}$, $C_{30}$ | 3-hourly | 3082472 | 11.2 | 1.018 | 1.119 |
| *GRACE-A data used for independent calibration* | | | | | | |
| NRLMSISE-00 | $C_{00}$ | Daily | 2987441 | 17.8 | 0.949 | 1.169 |
| NRLMSISE-00 | $C_{00}$ | 3-hourly | 2990681 | 17.7 | 0.941 | 1.160 |
| NRLMSISE-00 | $C_{00}$, $C_{10}$, $C_{20}$, $C_{30}$ | Daily | 2987441 | 19.1 | 0.938 | 1.176 |
| NRLMSISE-00 | $C_{00}$, $C_{10}$, $C_{20}$, $C_{30}$ | 3-hourly | 2989601 | 19.1 | 0.925 | 1.164 |

nal, uncalibrated model in the top-right panel greatly overestimated the density during the storm, the calibration with a single scale factor brings the model and data to the same level, changing the log-normal mean from $\mu* = 0.537$ to 1.011 and 0.996 when calibrating with CHAMP or GRACE data, respectively. The addition of additional zonal harmonics in the calibration using CHAMP data further improves the fit between the model and data, as is to be expected. However, the adjustment using the independent GRACE data only results in a better fit when estimating the single scale factor. The addition of the three additional zonal harmonic coefficients changes the offset from the mean and the standard deviation slightly, from $\mu^* = 0.996$ to 0.971 and from $\sigma^* = 1.187$ to 1.200, as shown in the figure. This degradation is likely due to the different sampling of the diurnal bulge, due to the difference in local solar time of both satellite tracks at these dates. By calibrating using the zonal spherical harmonics, the different shape of the bulge as sensed by GRACEA at 01:00/13:00 LST, is imposed on the model evaluated for CHAMP at 04:00/16:00 LST.

### Evaluation of the Calibration Along CHAMP and GRACE Tracks Over the Year 2003

For both CHAMP and GRACE-A, the various calibrated models have been evaluated using statistics over the entire year 2003 as well. The results are presented in Tables 6.5 and 6.6.

These tables contain four sections. The top two sections shows the statistics for the uncalibrated NRLMSIS-00 and JB2008 models, as well as for the independent HASDM data. These data, especially the uncalibrated NRLMSIS-00 statistics, serve

**Table 6.6** Statistics of calibrated density model output, evaluated along the GRACE-A orbit, over the year 2003. The column headings are the same as in the previous table

| Base model | Parameters | Interval | N | $E$ (%) | $\mu^*$ | $\sigma^*$ |
|---|---|---|---|---|---|---|
| *Uncalibrated* | | | | | | |
| NRLMSISE-00 | – | – | 2313350 | 45.9 | 0.834 | 1.332 |
| JB-2008 | – | – | 2313350 | 28.8 | 0.913 | 1.254 |
| *HASDM calibrated model using SSN data* | | | | | | |
| HASDM | Custom | 3-hourly | 2313350 | 22.4 | 0.909 | 1.186 |
| *GRACE-A data used for calibration* | | | | | | |
| NRLMSISE-00 | $C_{00}$ | Daily | 2313339 | 18.8 | 1.052 | 1.211 |
| NRLMSISE-00 | $C_{00}$ | 3-hourly | 2313339 | 17.4 | 1.044 | 1.193 |
| NRLMSISE-00 | $C_{00}$, $C_{10}$, $C_{20}$, $C_{30}$ | Daily | 2313339 | 16.5 | 1.040 | 1.185 |
| NRLMSISE-00 | $C_{00}$, $C_{10}$, $C_{20}$, $C_{30}$ | 3-hourly | 2312521 | 13.5 | 1.027 | 1.149 |
| *CHAMP data used for independent calibration* | | | | | | |
| NRLMSISE-00 | $C_{00}$ | Daily | 2300108 | 20.8 | 1.140 | 1.215 |
| NRLMSISE-00 | $C_{00}$ | 3-hourly | 2299344 | 19.9 | 1.134 | 1.202 |
| NRLMSISE-00 | $C_{00}$, $C_{10}$, $C_{20}$, $C_{30}$ | Daily | 2307304 | 20.0 | 1.137 | 1.206 |
| NRLMSISE-00 | $C_{00}$, $C_{10}$, $C_{20}$, $C_{30}$ | 3-hourly | 2299344 | 18.4 | 1.128 | 1.185 |

as a reference for the improvement that the calibration can bring. The evaluation of the HASDM model was included in order to be able to compare whether the calibration with accelerometer data from just one mission can compete with the calibration using many radar-tracked calibration objects.

The third section contains the results of the calibration using data from the same satellite as is used in the evaluation. This is, of course, not a fair evaluation of the benefits of the calibration, but these statistics are included in order to evaluate the limits of the parameterisation that are used. For example, the log-normal means of the data/model density ratios is within 2CHAMP and within 3exactly equal to one, because the data are weighted in the calibration, and not in the evaluation. The standard deviations decrease significantly with the introduction of additional calibration parameters, as expected. However, only in the case of the estimation of four zonal harmonic parameters over 3-hourly time intervals, do the calibrated models outperform HASDM. And this is when the same data are used for calibration and evaluation, while the HASDM calibration is done with independent data. This result serves as an excellent example of the validity of the HASDM data.

The fourth section in these two tables shows the results for the calibration with independent accelerometer data from the mission (CHAMP or GRACEA) that was not used in the evaluation. As expected, these are somewhat worse than in the case where the same data are used both for evaluation and calibration. Still, a very significant improvement over the uncalibrated NRLMSIS-00 model is seen.

In the case of the evaluation along the GRACEA track, the calibrated model using only CHAMP data results in only a slightly lower standard deviation (1.185) than the HASDM model (1.186), which is calibrated using many radar-tracked objects.

Nevertheless, this demonstrates the validity of the CHAMP data for improving thermospheric density modelling.

The GRACEA-calibrated model, evaluated along the CHAMP trajectory, on the other hand, does not exceed the performance of HASDM (1.164 vs. 1.144). This result is not unexpected, since it was shown in the previous chapters that density data from observations at altitudes above about 450 km, both from the GRACE accelerometers and from TLE s, are not as accurate as equivalent data obtained at altitudes comparable to that of CHAMP, due to the relatively low drag signal.

It would be interesting to evaluate the performance of CHAMP and GRACE calibrated models in the orbit determination of higher altitude satellites, such as ERS-2, Envisat and CryoSat. Perhaps the higher altitude GRACE data will bring in more value there. Another exciting possibility for future investigations is the calibration of density models using combined data from accelerometers and TLE data. As recommended by an earlier feasibility study for ESA/ESOC [6, 9], these two data types could complement each other. The accelerometer data provides high temporal and spatial resolution along a narrow satellite track, while TLE-derived densities could provide global spatial coverage, if enough calibration objects are available, albeit at a much lower temporal resolution. The cross-calibration of such data sets would be an interesting investigation by itself.

## References

1. Bevington PR, Robinson DK (2003) Data reduction and error analysis for the physical sciences, 3rd edn. McGraw-Hill, New York
2. Bowman BR (2002) True satellite ballistic coefficient determination for HASDM. In: AIAA/AAS astrodynamics specialist conference and exhibit, 5–8 August 2002, Monterey, California AIAA 2002-4887
3. Bowman BR, Storz MF (2002) Time series analysis of HASDM thermospheric temperature and density corrections. In: AIAA/AAS astrodynamics specialist conference and exhibit, 5–8 August 2002, Monterey, California AIAA 2002-4890
4. Bowman BR, Storz MF et al (2003) High accuracy satellite drag model (HASDM) review. In: Lafontaine J (eds) Astrodynamics 2003 vol 116 of advances in the astronautical sciences. Univelt Inc, San Diego AAS 03-625
5. Casali SJ, Barker WN (2002) Dynamic calibration atmosphere (DCA) for the high accuracy satellite drag model (HASDM). In: AIAA/AAS astrodynamics specialist conference and exhibit, 5–8 August 2002, Monterey, California AIAA 2002-4888
6. Doornbos E (2004) Calibrated high accuracy satellite drag model—ESOC contract 16643/02/D/HK(SC) final report. Faculty of Aerospace Engineering Delft University of Technology, Delft, The Netherlands
7. Doornbos E (2006) NRTDM final report—Near Real-Time Density Model (NRTDM)—ESOC contract 18576/04/D/HK(SC). Delft Institute for Earth-Oriented Space Research
8. Doornbos E (2007) Thermosphere density model calibration in Space weather research towards applications in Europe. In: Lilensten J (ed) Astrophysics and space science library, vol 344. Springer, Dordrecht
9. Doornbos EN, Klinkrad H, Visser PNAM (2005) Atmospheric density calibration using satellite drag observations. Adv Space Res 36:515–521. doi:10.1016/j.asr.2005.02.009

10. Doornbos E, Klinkrad H, Scharroo R, Visser P (2007) Thermosphere density model calibration in the orbit determination and prediction of ERS-2 and Envisat. In: Lacoste H (ed) Envisat symposium Montreux, Switzerland, 23–27 April 2007, ESA SP-636
11. Doornbos E, Klinkrad H, Visser P (2008) Use of two-line element data for thermosphere neutral density model calibration. Adv Space Res 41(7 ):1115–1122. doi:10.1016/j.asr.2006.12.025
12. Doornbos E, Förster M, Fritsche B, van Helleputte T, van den IJssel J, Koppenwallner G, Lühr H, Rees D, Visser P (2009) ESTEC contract 21022/07/NL/HE air density models derived from multi-satellite drag observations—final report, DEOS / TU Delft scientific report 01/2009, TU Delft
13. Emmert JT, Meier RR, Picone JM, Lean JL, Christensen AB (2006) Thermospheric density 2002–2004: TIMED/GUVI dayside limb observations and satellite drag. J Geophys Res 111(A10S16). doi:10.1029/2005JA011495
14. Emmert JT, Picone JM, Meier RR (2008) Thermospheric global average density trends, 1967–2007, derived from orbits of 5000 near-earth objects. Geophys Res Lett 35(L05101). doi:10.1029/2007GL032809
15. Emmert JT, Lean JL, Picone JM (2010) Record-low thermospheric density during the 2008 solar minimum. Geophys Res Lett 37(L12102). doi:10.1029/2010GL043671
16. Förste C, Flechtner F, Schmidt R, Meyer U, Stubenvoll R, Barthelmes F, König R, Neumayer KH, Rothacher M, Reigber Ch, Biancale R, Bruinsma S, Lemoine J-M, Raimondo JC (2005) A new high resolution global gravity field model derived from combination of GRACE and CHAMP mission and altimetry/gravimetry surface gravity data. In: EGU general assembly 2005 Vienna, Austria, 24-29 April 2005
17. Lean JL, Picone JM, Emmert JT, Moore G (2006) Thermospheric densities derived from spacecraft orbits. Application to the Starshine satellites. J Geophys Res 111(A04301). doi:10.1029/2005JA011399
18. Moré JJ, Garbow BS, Hillstrom KE (1980) User guide for MINPACK-1 Argonne National Laboratory, Argonne, Illinois ANL-80-74
19. Olver FWJ, Lozier DW, Boisvert RF, Clark CW (eds) (2010) NIST handbook of mathematical functions. Cambridge University Press, Cambridge
20. Press WH, Teukolsky SA, Vetterling WT, Flannery BP (2007) Numerical recipes—the art of scientific computing, 3rd edn. Cambridge University Press, Cambridge
21. Scharroo R, Pieter V (1998) Precise orbit determination and gravity field improvement for the ERS satellites. J Geophys Res 103(C4):8113–8127
22. Tapley BD, Watkins MM, Ries JC, Davis GW, Eanes RJ, Poole SR, Rim HJ, Schutz BE, Shum CK, Nerem RS, Lerch FJ, Marshall JA, Klosko SM, Pavlis NK, Williamson RG (1996) The joint gravity model 3. J Geophys Res 101(B12):28,029–28,049. doi:10.1029/96JB01645
23. Yurasov VS, Nazarenko AI, Cefola PJ, Alfriend KT (2005) Density corrections for the NRLMSIS-00 atmosphere model. In: AAS/AIAA Space Flight mechanics conference. Copper Mountain, Colorado, January 23–27 2005, AAS 05-168